

Thermochemistry of $\text{La}_{0.7}\text{Sr}_{0.3}\text{Mn}_{1-x}\text{Fe}_x\text{O}_3$ solid solutions ($0 < x < 1$)

Nihan Kemik ^{a,b}, Yayoi Takamura ^a, Alexandra Navrotsky ^{a,b,*}

^a Department of Chemical Engineering and Materials Science, University of California, Davis, CA 95616, United States

^b Peter A. Rock Thermochemistry Laboratory and Nanomaterials in the Environment, Agriculture & Technology Organized Research Unit (NEAT ORU), University of California, Davis, CA 95616, United States

ARTICLE INFO

Article history:

Received 18 February 2011

Received in revised form

24 May 2011

Accepted 29 May 2011

Available online 7 June 2011

Keywords:

Perovskite

Transition metal oxide

$(\text{La},\text{Sr})\text{MnO}_3$

$(\text{La},\text{Sr})\text{FeO}_3$

Calorimetry

Thermodynamics

ABSTRACT

The structure, the energetics and the internal redox reactions of $\text{La}_{0.7}\text{Sr}_{0.3}\text{Fe}_x\text{Mn}_{1-x}\text{O}_3$ have been studied in the complete solid solution range $0.0 < x < 1.0$. High temperature oxide melt drop solution calorimetry was performed to determine the enthalpies of formation from binary oxides and the enthalpy of mixing. There is a noticeable change in the energetics of the solid solution near $x=0.7$, which is due to the growing concentration of Fe^{4+} at higher $\text{Fe}/(\text{Fe}+\text{Mn})$ ratio. The balance between different valences of the transition metals, Mn and Fe, is the main factor in determining the energetics of the $\text{La}_{0.7}\text{Sr}_{0.3}\text{Fe}_x\text{Mn}_{1-x}\text{O}_3$ solid solution.

Published by Elsevier Inc.

1. Introduction

Transition metal oxides with the perovskite structure (ABO_3) exhibit a variety of interesting properties such as high temperature superconductivity [1], ferroelectricity [2–4] and ferromagnetism [5–7]. $(\text{La},\text{Sr})\text{MnO}_3$ and $(\text{La},\text{Sr})\text{FeO}_3$ perovskites have been proposed as cathode materials in solid oxide fuel cells (SOFCs) due to their mixed ionic and electronic conductivity [8–12]. In addition, $\text{La}(\text{Sr})\text{MnO}_3$ has attracted scientific interest recently for its colossal magnetoresistive (CMR) and half metallic properties [6,13,14]. In $\text{La}_{(1-y)}\text{Sr}_y\text{MnO}_3$, doping of the trivalent A site (La ions) with divalent ions such as Sr^{2+} causes the oxidation of some of the Mn^{3+} to Mn^{4+} to form $\text{La}_{(1-y)}\text{Sr}_y(\text{Mn}^{3+})_{1-y}(\text{Mn}^{4+})_y\text{O}_3$. The hopping of electrons between mixed valence Mn^{3+} and Mn^{4+} through a bridging O^{2-} ion forms the basis of the double exchange mechanism [15,16], which controls the magnetic and electronic transport properties of these materials.

Thus far, most studies of these perovskites structures have investigated the effects of A site doping, which is typically accompanied by strong lattice strain effects. In contrast, doping on the B site with other transition metal ions is an interesting alternative way of modifying the B site valence state. For example,

lattice strain effects are minimal when $(\text{La},\text{Sr})\text{MnO}_3$ is doped with Fe since Fe^{3+} and Mn^{3+} have very similar ionic radii [17]. An early study by Jonker [18] showed that, in the $(\text{La},\text{Ba})\text{MnO}_3$ system, the difference in the fourth ionization energy of Mn and Fe causes Mn^{3+} to be directly replaced by Fe^{3+} without the formation of Fe^{4+} ions up to a certain critical Fe concentration. This critical concentration is dictated by the extent of divalent doping on the A site. Ahn et al. [19,20] showed that, in $(\text{La},\text{Ca})\text{MnO}_3$, Fe doping (< 20%) depopulates the hopping electrons, weakens the double exchange interaction and consequently reduces the conductivity and ferromagnetism. Several other studies have also reported similar behavior for low Fe doping in $(\text{La},\text{Sr})\text{MnO}_3$ [21,22]. From these studies, it is clear that the electronic and magnetic properties of these materials depend strongly on the interaction between Mn and Fe ions with different valence states. In this paper, we have investigated the thermodynamics of the complete solid solution of the Fe doped $\text{La}_{0.7}\text{Sr}_{0.3}\text{MnO}_3$ system by oxide melt solution calorimetry in order to understand how the valence state of the transition metal ion affects the structure and energetics.

In general, the energetics in perovskites indicate that the structure becomes less stable as the size (basicity) of the A site cation decreases and the Goldschmidt tolerance factor [23] deviates from unity [24]. In Mn perovskites such as LaMnO_3 , YMnO_3 , NdMnO_3 and $\text{La}_{1-y}\text{Sr}_y\text{MnO}_3$, the stability decreases as the size of the divalent and/or trivalent A site cation decreases [25]. A thermodynamic study of $\text{La}_{1-y}\text{Sr}_y\text{FeO}_3$ by Cheng et al. [26] suggests that, at low Sr concentrations, the system becomes less

* Corresponding author at: Department of Chemical Engineering and Materials Science, University of California, Davis, CA 95616, United States.

E-mail address: anavrotsky@ucdavis.edu (A. Navrotsky).

stable due to oxygen vacancy formation, whereas the enthalpy of formation becomes constant around $y=0.50$ due to oxygen vacancy ordering. For end-member LaMO_3 ($M=\text{Cr, Fe, Co, Ni}$) perovskites, the stability of the structure decreases in the order of Cr, Fe, Co and Ni [27]. Within this series, the energetics cannot be explained by the tolerance factor alone, and the electronic configuration of the B site cation and its valence state must also be considered.

The Fe doped $\text{La}_{0.7}\text{Sr}_{0.3}\text{MnO}_3$ system is an ideal system to study the redox reactions between Mn^{3+} , Mn^{4+} , Fe^{3+} and Fe^{4+} without changing the tolerance factor of the perovskite. From a practical point of view, thermodynamic data are essential to predict the stability of materials in high temperature applications such as SOFC. Fundamentally, thermodynamic data give insight into the interactions among different valence states of Mn and Fe ions in the solid solution. In this study, we utilize high temperature oxide melt solution calorimetry to obtain the energetics of the Fe doped $\text{La}_{0.7}\text{Sr}_{0.3}\text{MnO}_3$ solid solution, that is, the $\text{La}_{0.7}\text{Sr}_{0.3}\text{Fe}_x\text{Mn}_{1-x}\text{O}_3$ series.

2. Experimental methods

2.1. Synthesis and characterization

$\text{La}_{0.7}\text{Sr}_{0.3}\text{MnO}_3$ and $\text{La}_{0.7}\text{Sr}_{0.3}\text{FeO}_3$ bulk samples synthesized by combustion spray pyrolysis were obtained from Praxair Specialty Ceramics. The solid solution compositions, $\text{La}_{0.7}\text{Sr}_{0.3}\text{Mn}_{1-x}\text{Fe}_x\text{O}_3$ ($x=0.25, 0.5, 0.75$ and 0.9), were synthesized by solid state reaction of stoichiometric mixture of the end-members $\text{La}_{0.7}\text{Sr}_{0.3}\text{MnO}_3$ and $\text{La}_{0.7}\text{Sr}_{0.3}\text{FeO}_3$ at $1500\text{ }^\circ\text{C}$ for 15 h.

X-ray diffraction (XRD) patterns were collected using a Bruker AXS D8 Advance diffractometer operated at an accelerating voltage of 40 kV and an emission current of 40 mA with $\text{CuK}\alpha_1$ radiation ($\lambda=1.5406\text{ \AA}$). Data were collected from 20° to 90° in 2θ using a step size of 0.02° and 0.03 s collection time. Whole pattern fitting as implemented in MDI Jade software was used to refine the lattice parameters.

Chemical analyses were performed by wavelength dispersive spectroscopy (WDS) using a Cameca SX-100 electron microprobe

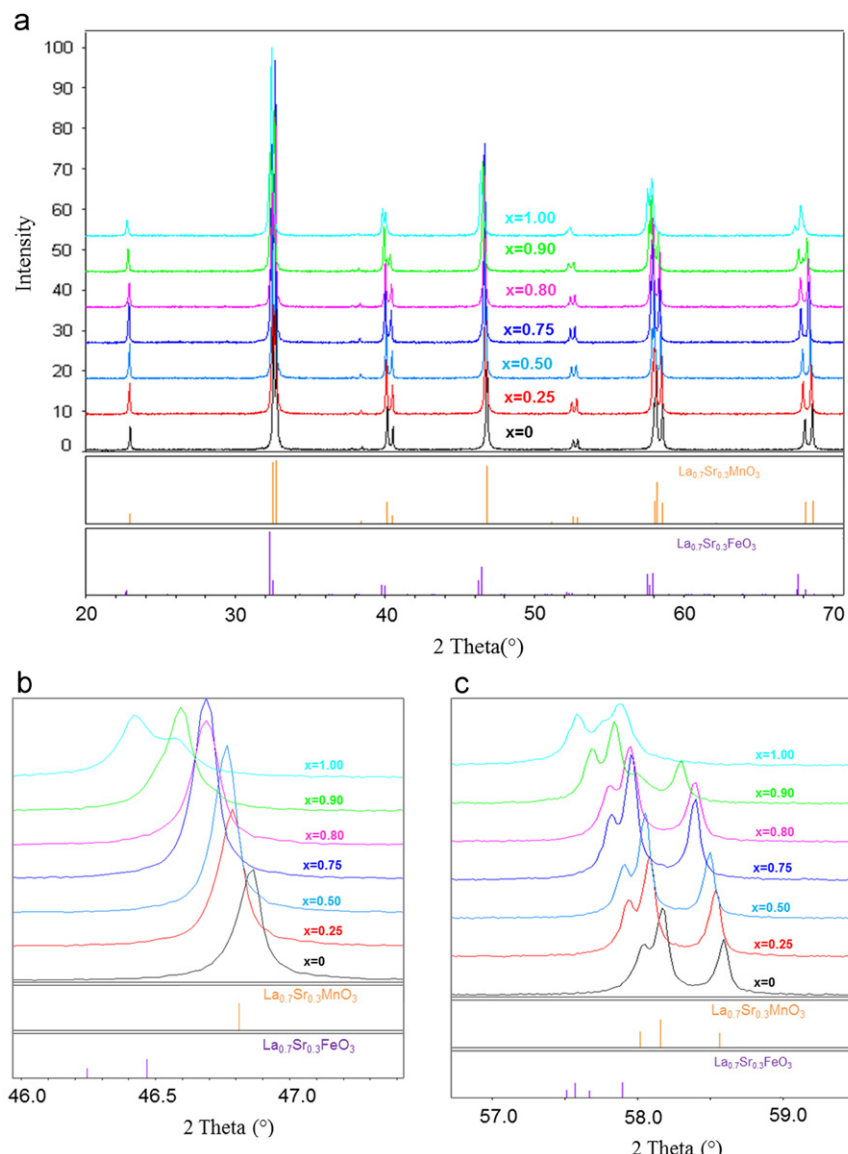


Fig. 1. XRD patterns of the $\text{La}_{0.7}\text{Sr}_{0.3}\text{Mn}_{1-x}\text{Fe}_x\text{O}_3-\gamma$ solid solution series. The reference powder diffraction data of $\text{La}_{0.7}\text{Sr}_{0.3}\text{MnO}_3$ (#50712) and $\text{La}_{0.7}\text{Sr}_{0.3}\text{FeO}_3$ (#86126) are given as marked lines, (b) and (c) zoomed in patterns around $2\theta=47^\circ$ and 58° .

with an accelerating voltage of 15 kV, a beam current of 20 nA and a beam size of 1 μm . LaPO₄, SrTiO₃, Fe₂O₃ and Mn metal were used as standards. An average of 12 points was used to determine the sample composition. Homogeneity and impurity content were examined by X-ray dot mapping and backscattered electron images.

Oxygen content was determined from thermogravimetric analysis (TGA) using a Setaram Labsys system. Before each run, the chamber was purged with the desired gas for an hour at a high flow of 200 mL/min, followed by the normal flow rate of 40 mL/min to ensure the purity of the gas during the run. The samples were first heated in Ar atmosphere to 700 °C at 5 °C/min and cooled to room temperature at 10 °C/min. Then the samples were reheated to 900 °C at 5 °C/min and cooled to room temperature in O₂ atmosphere at 10 °C/min. For each run, the crucible was weighed before and after TG measurements using a microbalance to determine the weight loss/gain. These runs were repeated once to confirm that the weight loss/gain values were consistent.

2.2. High temperature oxide melt solution calorimetry

High temperature drop solution calorimetry was performed in a custom built twin Calvet type microcalorimeter and has been described in detail previously by Navrotsky [28,29]. Samples were pressed into pellets (~8 mg), weighed on a microbalance and dropped from room temperature into solvent in the calorimeter at 702 °C. Lead borate (2PbO·B₂O₃) was the solvent and air was bubbled through it (5.5 mL/min) to stir the melt and help dissolve the samples completely and prevent local saturation of the solvent. Air was also flushed through the calorimeter glassware assembly at 60 mL/min. Under these conditions, all dissolved iron and manganese were in the trivalent state, as shown previously [26]. The heat effect (drop solution enthalpy, ΔH_{ds}) includes the heat content, the enthalpy of dissolution of oxides and the enthalpy associated with the reduction of Mn⁴⁺ and Fe⁴⁺ present in the samples to +3 valence states in the solvent. The calorimeter was calibrated using the heat content of 15 mg pellets of Al₂O₃.

3. Results

3.1. Structure and composition

The cation compositions (La, Sr, Mn and Fe) were confirmed by microprobe analysis. The actual compositions of the samples were within 1% of the nominal initial material compositions and no additional phases were found.

The XRD patterns of the La_{0.7}Sr_{0.3}Mn_{1-x}Fe_xO₃ solid solutions with different Fe contents are given in Fig. 1. The XRD patterns of the end members confirm that La_{0.7}Sr_{0.3}MnO₃ has a rhombohedral (R3c, #50712) and La_{0.7}Sr_{0.3}FeO₃ has an orthorhombic (Pbnm, #86126) distorted perovskite structure due to [MO₆] octahedral tilting. The tilting of the octahedra results in peak splitting in the XRD patterns compared to that of the ideal cubic perovskite structure. Furthermore, the extent of peak splitting is more pronounced in the Pbnm structure than the rhombohedral structure due to its lower symmetry (see Fig. 1b and c). For instance, the (024) reflection in the R3c structure is split into (004) and (220) reflections in Pbnm (Fig. 1b) near $2\theta=46.8^\circ$. Similarly, three reflections ((300), (214) and (018)) are found in the R3c structure and two wider peaks consisting of the superimposed (312), (204), (024) and (132) reflections are found in the Pbnm structure near $2\theta=58^\circ$ (Fig. 1c). We use the nature of these splitting features as a signature to assign the structures of the solid solution to either Pbnm or R3c space groups.

In the XRD patterns of the solid solution samples (Fig. 1a), the peaks shift towards lower 2θ values as the Fe concentration

Table 1

Crystal structure, lattice parameters and oxygen deficiency, γ , for the La_{0.7}Sr_{0.3}Mn_{1-x}Fe_xO_{3- γ} solid solution series.

Sample	Structure	Lattice parameters (Å)	γ
$x=0$	Rhombohedral	$a=5.509$ $c=13.362$	0
$x=0.25$	Rhombohedral	$a=5.515$ $c=13.368$	0
$x=0.5$	Rhombohedral	$a=5.520$ $c=13.381$	0
$x=0.75$	Rhombohedral	$a=5.527$ $c=13.401$	0.006
$x=0.80$	Rhombohedral	$a=5.530$ $c=13.408$	0.006
$x=0.90$	Rhombohedral, orthorhombic	$a=5.537$ $c=13.417$	$a=5.501$ $b=5.550$ $c=7.783$ 0.016
$x=1$	Orthorhombic	$a=5.515$ $b=5.554$ $c=7.802$	0.022

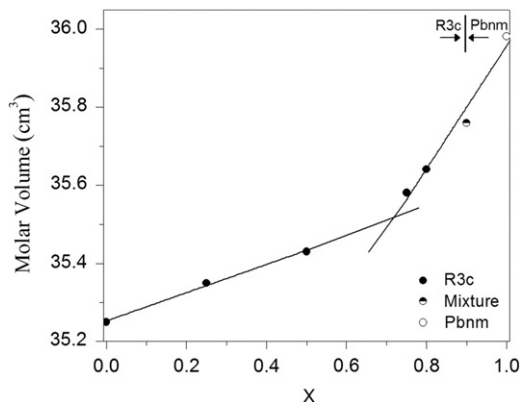


Fig. 2. Molar volume of the La_{0.7}Sr_{0.3}Mn_{1-x}Fe_xO_{3- γ} solid solution as a function of Fe/(Fe+Mn) ratio, x .

increases, indicating that the lattice parameters increase. The lattice parameters obtained by whole pattern refinement are given in Table 1. The nature of the peak splitting in the patterns indicates that the rhombohedral structure is preserved in the solid solution series up to $x=0.9$, where a mixture of the two structures is observed. This structure change must be a first order transition since the orthorhombic space group is not a sub-group of the rhombohedral space group. The variation of molar volume with composition is shown in Fig. 2.

The absence of any significant weight loss in the TGA data indicates negligible surface adsorbed water in these samples. A small weight loss (<0.25%) below 300 °C observed in the first Ar run is within the uncertainties of measurements. The oxygen stoichiometry was determined using the weight gain measured during the O₂ run. No significant weight gain occurred during the O₂ runs for samples below $x=0.75$, indicating that these samples are oxygen stoichiometric. The samples with $0.75 < x < 1.00$ showed a small amount of oxygen deficiency, γ , as listed in Table 1.

3.2. Calorimetry

The calorimetric data are summarized in Table 2. Using the thermodynamic cycle in Table 3, we calculated the enthalpy of formation from binary oxides (Mn₂O₃, Fe₂O₃, La₂O₃ and SrO) plus oxygen for these perovskites at room temperature. Mn and Fe in Mn₂O₃ and Fe₂O₃ are in the +3 state and they remain as +3 ions upon dissolution in molten lead borate solvent during

calorimetric measurements. However, Mn^{4+} and Fe^{4+} are also present in the Sr doped perovskites and hence the dissolution of these compounds in lead borate solvent also involves the reduction of these +4 ions to their +3 valence states. Thus, the thermodynamic cycle given in Table 3 gives not only the enthalpy of formation but also a combination of the enthalpy of formation and the enthalpy of oxidation. These results are plotted as a function of x in Fig. 3. The enthalpy of mixing (ΔH_{mix}) for the solid solution is calculated using the drop solution enthalpies of the end members and is plotted versus x in Fig. 4.

Figs. 2–4 show that the volumes and enthalpies deviate strongly from a linear relationship between the end members, with substantial negative deviations from ideality in both volume and enthalpy. That is, the intermediate compositions show a smaller volume and a more favorable enthalpy than a mixture of $La_{0.7}Sr_{0.3}MnO_3$ and $La_{0.7}Sr_{0.3}FeO_3$. Both the enthalpy and the volume data are better represented by two straight line segments intersecting near $x=0.7$ than by a quadratic or cubic polynomial. This result suggests that a marked change in behavior occurs near

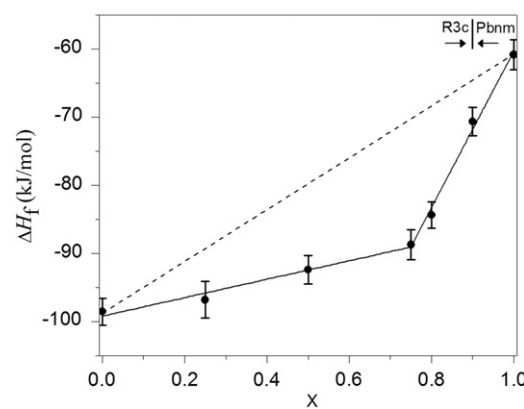


Fig. 3. Enthalpy of formation (ΔH_f) from binary oxides (La_2O_3 , Fe_2O_3 , Mn_2O_3 and SrO) plus oxygen for $La_{0.7}Sr_{0.3}Mn_{1-x}Fe_xO_{3-\gamma}$ perovskites at room temperature as a function of $Fe/(Fe + Mn)$ ratio, x . The dashed line shows the formation enthalpy of a mechanical mixture of the end members. Linear fits for the two regions at low and high x are shown as solid lines.

Table 2
Thermochemical data for the $La_{0.7}Sr_{0.3}Mn_{1-x}Fe_xO_{3-\gamma}$ perovskites.

Sample	ΔH_{ds} (kJ/mol)	ΔH_f (kJ/mol)
La_2O_3	43.11 ± 4.5^a	
Mn_2O_3	146.6 ± 1.84^b	
Fe_2O_3	170.59 ± 1.29^c	
SrO	58.07 ± 1.90^d	
$x=0$	$144.89 \pm 0.83(5)^e$	-98.55 ± 1.98
$x=0.25$	$145.18 \pm 2.03(13)$	-96.82 ± 2.68
$x=0.50$	$142.78 \pm 1.16(8)$	-92.40 ± 2.06
$x=0.75$	$141.09 \pm 1.33(8)$	-88.75 ± 2.20
$x=0.80$	$137.09 \pm 0.80(8)$	-84.35 ± 1.93
$x=0.90$	$124.08 \pm 1.06(8)$	-70.64 ± 2.07
$x=1$	$115.01 \pm 1.31(10)$	-60.83 ± 2.22

^a Cheng et al. [30].

^b Navrotsky et al. [34].

^c Majzlan et al. [35].

^d Cheng et al. [26].

^e Uncertainty is two standard deviation of the mean; the number in the parenthesis is the number of drops.

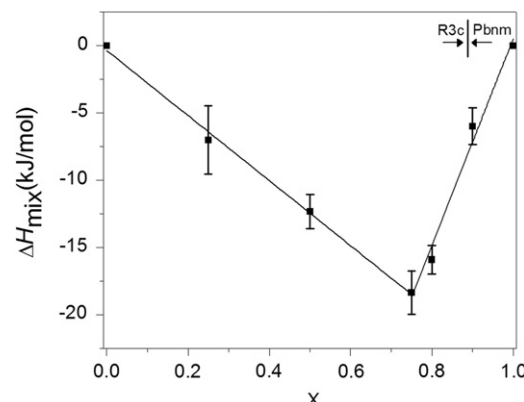


Fig. 4. Enthalpy of mixing (ΔH_{mix}) of $La_{0.7}Sr_{0.3}Mn_{1-x}Fe_xO_{3-\gamma}$ solid solution at room temperature as a function of $Fe/(Fe + Mn)$ ratio, x . Linear fits for the two regions at low and high x are shown as solid lines.

Table 3

Thermochemical cycle for enthalpies of formation from oxides for the $La_{0.7}Sr_{0.3}Mn_{1-x}Fe_xO_{3-\gamma}$ perovskites at room temperature.

Reaction	ΔH
La_2O_3 (xl, 25 °C) \rightarrow La_2O_3 (sol, 702 °C) ^a	$\Delta H (1) = \Delta H_{ds} (La_2O_3)$
Mn_2O_3 (xl, 25 °C) \rightarrow Mn_2O_3 (sol, 702 °C)	$\Delta H (2) = \Delta H_{ds} (Mn_2O_3)$
Fe_2O_3 (xl, 25 °C) \rightarrow Fe_2O_3 (sol, 702 °C)	$\Delta H (3) = \Delta H_{ds} (Fe_2O_3)$
SrO (xl, 25 °C) \rightarrow SrO (sol, 702 °C)	$\Delta H (4) = \Delta H_{ds} (SrO)$
O_2 (g, 25 °C) \rightarrow O_2 (g, 702 °C)	$\Delta H (5) = \Delta H_{25-702} (O_2)$ ^b
$La_{0.7}Sr_{0.3}Mn_{1-x}Fe_xO_{3-\gamma}$ (xl, 25 °C) \rightarrow	$\Delta H (6) = \Delta H_{ds} (La_{0.7}Sr_{0.3}Mn_{1-x}Fe_xO_{3-\gamma})$
$0.35 La_2O_3$ (sol, 702 °C) $+ \frac{1-x}{2} Mn_2O_3$ (sol, 702 °C)	
$+ \frac{x}{2} Fe_2O_3$ (sol, 702 °C) $+ 0.3 SrO$ (sol, 702 °C) $+ \frac{0.15-\gamma}{2} O_2$ (g, 702 °C)	
$0.35 La_2O_3$ (xl, 25 °C) $+ \frac{1-x}{2} Mn_2O_3$ (xl, 25 °C)	$\Delta H (7) = \Delta H_f (La_{0.7}Sr_{0.3}Mn_{1-x}Fe_xO_{3-\gamma})$
$+ \frac{x}{2} Fe_2O_3$ (xl, 25 °C) $+ 0.3 SrO$ (xl, 25 °C)	
$+ \frac{0.15-\gamma}{2} O_2$ (g, 25 °C) $\rightarrow La_{0.7}Sr_{0.3}Mn_{1-x}Fe_xO_{3-\gamma}$ (xl, 25 °C)	
$\Delta H(7) = 0.35\Delta H(1) + \frac{1-x}{2}\Delta H(2) + \frac{x}{2}\Delta H(3) + 0.3\Delta H(4) + \frac{0.15-\gamma}{2}\Delta H(5) - \Delta H(6)$	

^a xl=crystalline solid, g=gas, sol=solution in $2PbO \cdot B_2O_3$.

^b Heat content of O_2 from 25 to 702 °C, calculated from Robie and Hewingway [36], 21.86 kJ/mol.

$x=0.7$. This is attributed to the growing concentration of Fe^{4+} at higher $\text{Fe}/(\text{Fe}+\text{Mn})$ values (see below). We note that $x=0.7$ lies well within the region of Fe doping where the rhombohedral ($R3c$) phase is observed, with the transition to orthorhombic ($Pbnm$) occurring at $x=0.9$. This transition is seen as a small effect in the volumetric data (Fig. 2) but not in the energetics (Figs. 3 and 4). The absence of any effect bigger than experimental error in the energetics at $x=0.9$ suggests that the enthalpy of the $R3c$ to $Pbnm$ transition is small (2 kJ/mol in magnitude), consistent with the data for other perovskite distortional transitions [30]. Thus the pronounced change near $x=0.7$ is not related to the symmetry change.

4. Discussion

Both $\text{La}_{0.7}\text{Sr}_{0.3}\text{MnO}_3$ and $\text{La}_{0.7}\text{Sr}_{0.3}\text{FeO}_3$ belong to the distorted cubic perovskite family. Distorted cubic perovskite structures occur not only due to octahedral tilting but also due to the Jahn–Teller distortions. The Jahn–Teller distortion results from an odd number of electrons in the e_g orbitals and can be observed in the d^4 electron configuration seen in Mn^{3+} and Fe^{4+} . Fe^{3+} (d^5) and Mn^{4+} (d^3) have five and three electrons in their d shells, respectively, therefore they prefer a symmetric structure. The $R3c$ structure does not have long-range cooperative Jahn–Teller distortion, whereas in the orthorhombic $Pbnm$ structure these effects are dominant [31].

Jonker [18] established a diagram showing Mn and Fe ions in different valence states in the Fe doped $\text{La}_{0.85}\text{Ba}_{0.15}\text{MnO}_3$ system. We constructed a similar diagram for the $\text{La}_{0.7}\text{Sr}_{0.3}\text{Mn}_{1-x}\text{Fe}_x\text{O}_3$ solid solution studied here (Fig. 5) with a divalent dopant concentration of 0.3. According to this diagram, the Mn^{4+} concentration remains constant up to a certain point, as Mn^{3+} is substituted directly for Fe^{3+} in the $\text{La}_{0.7}\text{Sr}_{0.3}\text{Mn}_{1-x}\text{Fe}_x\text{O}_3$ solid solution. At $x=0.7$, Fe^{4+} begins to form because of the abundance of Fe and the necessity for charge balance. In this region, Mn^{4+} is substituted by Fe^{4+} with increase in x and the Fe^{3+} concentration remains constant. It is important to note that these concentrations are only valid if the samples are completely oxygen stoichiometric. Using this diagram, we can explain the behavior of the solid solution crystal structure as a function of x . As Fe^{3+} is substituted for Mn^{3+} , because the two ions have nearly identical radii (0.65 Å) [17] and Fe^{3+} has a symmetric electronic structure, the rhombohedral structure is retained without any further distortion of the octahedra. As x reaches 0.7, the Jahn–Teller distorted Fe^{4+} ion starts to form in significant amounts and the

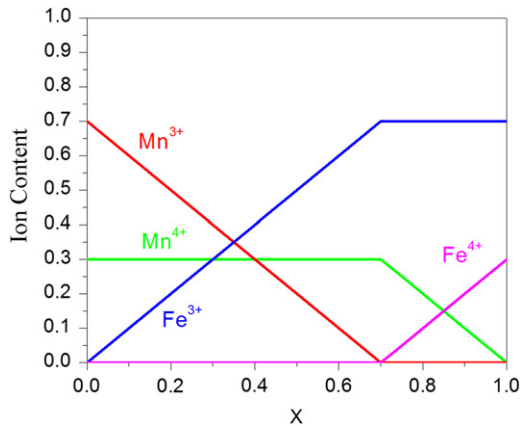
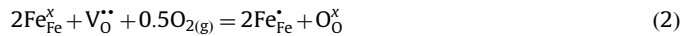
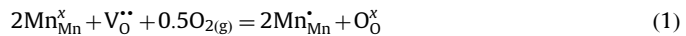


Fig. 5. Contents of Mn^{3+} , Mn^{4+} , Fe^{3+} and Fe^{4+} upon Fe doping in $\text{La}_{0.7}\text{Sr}_{0.3}\text{Mn}_{1-x}\text{Fe}_x\text{O}_3$ stoichiometric solid solution as a function of $\text{Fe}/(\text{Fe}+\text{Mn})$ ratio, x , based on Jonker's work [18].

interaction between Fe^{4+} and Mn^{4+} pushes the rhombohedral to orthorhombic transition to higher Fe^{4+} content. This competition explains the dominance of the rhombohedral structure up to $x=0.9$ (Fig. 1) and the mixture of the rhombohedral and orthorhombic structures at $x=0.9$ (Fig. 1(c)). Pure LSFO in the absence of Mn^{4+} is purely orthorhombic with the Jahn–Teller distortion. These observations demonstrate that both Jahn–Teller distortions and redox behavior/reaction between $\text{Mn}^{3+}/\text{Mn}^{4+}$ and $\text{Fe}^{3+}/\text{Fe}^{4+}$ influence the formation of different perovskite structures in the $\text{La}_{0.7}\text{Sr}_{0.3}\text{Mn}_{1-x}\text{Fe}_x\text{O}_{3-\gamma}$ solid solution.

Thermodynamic data also reflect the influence of the Jahn–Teller distortions and redox behavior on the stability of different phases in the $\text{La}_{0.7}\text{Sr}_{0.3}\text{Mn}_{1-x}\text{Fe}_x\text{O}_{3-\gamma}$ solid solution. In Fig. 3, the dashed line indicates the energetics for the mechanical mixture of the end members. The enthalpy of formation shows a negative deviation from this line, which indicates the stabilization of the solid solution. Furthermore, the data can be approximated by two linear regimes: $0 < x < 0.7$ and $0.7 < x < 1$. In the first region, the enthalpy of formation becomes more endothermic upon Fe substitution at a slower rate compared to the second region. A polynomial does not fit the data well.

In order to separate the effects of oxidation and formation on these materials, it is essential to know the defect equations for the oxidation of Mn^{3+} and Fe^{3+} and the enthalpy of oxidation values for these perovskites. The oxidation reactions in which the oxidation of +3 ions to +4 ions is accompanied by the filling of oxygen vacancies can be represented by the following defect equations:



The Kroger–Vink notation is taken in these defect equations where the major defects are $\text{V}_0^{\bullet\bullet}$, $2\text{Mn}_{\text{Mn}}^{\bullet}$ (Mn^{4+}) and $2\text{Fe}_{\text{Fe}}^{\bullet}$ (Fe^{4+}). Fritsch and Navrotsky [32] calculated the enthalpy of oxidation of Mn_2O_3 to MnO_2 as -316.8 ± 14 kJ/(mol. of O_2). Mizusaki et al. [33] found the enthalpy of oxidation for 30% Sr doped LaFeO_3 to be -230.22 ± 31.8 kJ/(mol. of O_2). From these data, we conclude that the enthalpy of oxidation for Mn is more exothermic than for Fe, therefore the oxidation of Mn^{3+} is favored over Fe^{3+} . This supports the diagram given in Fig. 5 based on Jonker's work [18]. These oxidation values and the corresponding ion concentrations from the diagram in Fig. 5 were used to calculate the enthalpy oxidation of +3 transition metal to +4 for the $\text{La}_{0.7}\text{Sr}_{0.3}\text{Mn}_{1-x}\text{Fe}_x\text{O}_{3-\gamma}$ solid solution. As shown in Fig. 6, the enthalpy of oxidation (ΔH_{ox}) shows a nonlinear trend as a function of x and the Fe oxidation is much less favorable compared to Mn oxidation. The enthalpy of oxidation per

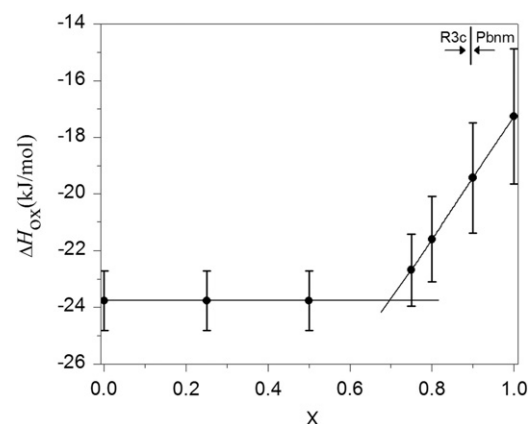


Fig. 6. Enthalpy of oxidation of +3 transition metal to +4 for $\text{La}_{0.7}\text{Sr}_{0.3}\text{Mn}_{1-x}\text{Fe}_x\text{O}_{3-\gamma}$ perovskites at room temperature as a function of $\text{Fe}/(\text{Fe}+\text{Mn})$ ratio, x .

mole O₂ in the regime 0 < x < 0.7 is a function of Mn oxidation and is constant since Mn⁴⁺ content does not change. At $x=0.7$, Fe⁴⁺ begins to form and the enthalpy of oxidation becomes a function of both Fe and Mn oxidation. Since Fe oxidation is more endothermic, a less exothermic enthalpy of oxidation is observed as Fe⁴⁺ concentration increases. By comparing Figs. 3 and 6, we find that the energetics of the La_{0.7}Sr_{0.3}Mn_{1-x}Fe_xO_{3- γ} solid solution is dominated by the oxidation reactions.

Fig. 4 shows the enthalpy of mixing (ΔH_{mix}) of La_{0.7}Sr_{0.3}Mn_{1-x}Fe_xO_{3- γ} solid solution at room temperature as a function of x . The enthalpies of mixing of the solid solution were calculated using the drop solution enthalpies of the end members and assuming that each composition is oxygen stoichiometric. Since the oxygen deficiency observed in Fe rich compositions is small, the effect of nonstoichiometry is within the error of the calculation. The enthalpies of mixing cannot be fit using a regular or subregular solution model. Instead, the enthalpy of mixing is better fit using two linear segments. In the first region, where the Mn³⁺ is substituted directly for Fe³⁺ and the concentration of Mn⁴⁺ remains constant, the line is represented by $\Delta H_{\text{mix}} = -0.28 - 24.66x$. In the second region where Fe⁴⁺ is substituted for Mn⁴⁺ and the Fe³⁺ concentration remains constant, the linear model gives $\Delta H_{\text{mix}} = -76.38 + 76.89x$. For low x , ΔH_{mix} becomes more exothermic as the Fe concentration increases and the ions with same valence and similar ionic sizes are substituted for each other. Therefore we see a favorable mixing behavior. The higher x region shows diminishing stabilization with increase in Fe content. In this region, we see multiple effects: unfavorable Fe⁴⁺ formation, the rhombohedral to orthorhombic transition and the formation of a small amount of oxygen vacancies. The destabilizing trend is probably mainly due to the formation of unfavorable Fe⁴⁺ ions. According to Jonker's diagram, Fe⁴⁺ formation becomes significant at $x=0.7$ for a completely oxygen stoichiometric composition. In our case, the samples with compositions $x \geq 0.75$ have small oxygen deficiencies, therefore, oxygen vacancy formation competes with Fe⁴⁺ formation and Fe⁴⁺ formation is pushed to higher concentrations. Formation of oxygen vacancies at the higher x region is not surprising. Cheng et al. [26] found that the enthalpy of oxidation is less exothermic at the higher Sr doping of LaFeO₃ compared to low Sr doping. It was suggested that as Fe⁴⁺ content increases, there is a stronger tendency to preserve the oxygen vacancies instead of forming more Fe⁴⁺ ions. In our system, oxygen vacancy formation in the higher x region stabilizes the system since it hinders the formation of Fe⁴⁺ ions. The energetic effect of the rhombohedral to orthorhombic transition observed in this regime appears to be very small and is within the error of the calculation. For LaBO₃ ($B=\text{Al}, \text{Ga}, \text{In}$ and Sc) perovskites, the enthalpy of transition from orthorhombic to rhombohedral structure was found as 0.17 kJ/mol from DSC measurements [30]. Thus, we conclude that the main factors governing the energetics of the solid solution at high x content is formation of Fe⁴⁺ ions and oxygen vacancies.

5. Conclusion

We have investigated the structure and energetics of the La_{0.7}Sr_{0.3}Mn_{1-x}Fe_xO₃ solid solution system. We found that the symmetry of the perovskite structure, the valence of transition metal and the energetics are highly interdependent. Oxidation of Mn³⁺ to Mn⁴⁺ is much more energetically favorable than oxidation of Fe³⁺ to Fe⁴⁺ and the redox reactions between different

valence states of Fe and Mn dominate the energetic behavior of the solid solution.

Acknowledgments

The authors thank the staff at Praxair Specialty Ceramic for supplying the samples and Radha Venkataramana and Tatiana Shvareva for insightful discussions of the calorimetric data. This work was supported by the Department of Energy (grant DEFG-02-03ER46053).

References

- [1] M.K. Wu, J.R. Ashburn, C.J. Torng, P.H. Hor, R.L. Meng, L. Gao, Z.J. Huang, Y.Q. Wang, C.W. Chu, *Physical Review Letters* 58 (1987) 908.
- [2] R. Ramesh, A. Inam, W.K. Chan, B. Wilkens, K. Myers, K. Remschnig, D.L. Hart, J.M. Tarascon, *Science* 252 (1991) 944–946.
- [3] N. Setter, D. Damjanovic, L. Eng, G. Fox, S. Gevorgian, S. Hong, A. Kingon, H. Kohlstedt, N.Y. Park, G.B. Stephenson, I. Stolitchnov, A.K. Taganov, D.V. Taylor, T. Yamada, S. Streiffer, *Journal of Applied Physics* 100 (2006) 051606–051646.
- [4] S.-W. Cheong, M. Mostovoy, *Nature Materials* 6 (2007) 13–20.
- [5] H.Y. Hwang, *MRS Bulletin* 31 (2006) 28–35.
- [6] A.P. Ramirez, *Journal of Physics—Condensed Matter* 9 (1997) 8171–8199.
- [7] S. Jin, T.H. Tiefel, M. McCormack, R.A. Fastnacht, R. Ramesh, L.H. Chen, *Science* 264 (1994) 413–415.
- [8] N.Q. Minh, *Journal of the American Ceramic Society* 76 (1993) 563–588.
- [9] J.M. Ralph, A.C. Schoeler, M. Krumpelt, *Journal of Materials Science* 36 (2001) 1161–1172.
- [10] S.J. Skinner, *International Journal of Inorganic Materials* 3 (2001) 113–121.
- [11] B.C.H. Steele, A. Heinzel, *Nature* 414 (2001) 345–352.
- [12] K. Huang, H.Y. Lee, J.B. Goodenough, *Journal of the Electrochemical Society* 145 (1998) 3220–3227.
- [13] K.-i. Chahara, T. Ohno, M. Kasai, Y. Kozono, *Applied Physics Letters* 63 (1993) 1990–1992.
- [14] A. Urushibara, Y. Moritomo, T. Arima, A. Asamitsu, G. Kido, Y. Tokura, *Physical Review B* 51 (1995) 14103–14109.
- [15] P.G. de Gennes, *Physical Review* 118 (1960) 141.
- [16] J.B. Goodenough, *Physical Review* 100 (1955) 564.
- [17] R. Shannon, *Acta Crystallographica Section A* 32 (1976) 751–767.
- [18] G.H. Jonker, *Physica* 20 (1954) 1118–1122.
- [19] K.H. Ahn, X.W. Wu, K. Liu, C.L. Chien, *Physical Review B* 54 (1996) 15299–15302.
- [20] K.H. Ahn, X.W. Wu, K. Liu, C.L. Chien, *Journal of Applied Physics* 81 (1997) 5505–5507.
- [21] A. Tiwari, K.P. Rajeev, *Journal of Applied Physics* 86 (1999) 5175–5178.
- [22] M.M. Xavier, F.A.O. Cabral, A. de, uacute, J.H. jo, C. Chesman, T. Dumelow, *Physical Review B* 63 (2000) 012408.
- [23] V.M. Goldschmidt, *Geochemische Verteilungsgesetze der Element* (1927–1928).
- [24] A. Navrotsky, *AIP Conference Proceedings* 535 (2000) 288–296.
- [25] C. Laberty, A. Navrotsky, C.N.R. Rao, P. Alphonse, *Journal of Solid State Chemistry* 145 (1999) 77–87.
- [26] J.J. Cheng, A. Navrotsky, X.D. Zhou, H.U. Anderson, *Chemistry of Materials* 17 (2005) 2197–2207.
- [27] J.H. Cheng, A. Navrotsky, X.D. Zhou, H.U. Anderson, *Journal of Materials Research* 20 (2005) 191–200.
- [28] A. Navrotsky, *Physics and Chemistry of Minerals* 2 (1977) 89–104.
- [29] A. Navrotsky, *Physics and Chemistry of Minerals* 24 (1997) 222–241.
- [30] J.H. Cheng, A. Navrotsky, X.D. Zhou, H.U. Anderson, *Journal of Materials Research* 18 (2003) 2501–2508.
- [31] L. Martin-Carron, A. Andres, M.J. Martinez-Lope, M.T. Casais, J.A. Alonso, *Physical Review B* 66 (2002) 174303.
- [32] S. Fritsch, A. Navrotsky, *Journal of the American Ceramic Society* 79 (1996) 1761–1768.
- [33] J. Mizusaki, M. Yoshihiro, S. Yamauchi, K. Fueki, *Journal of Solid State Chemistry* 58 (1985) 257–266.
- [34] A. Navrotsky, C. Ma, K. Lillova, N. Birkner, *Science* 330 (2010) 199–201.
- [35] J. Majzlan, A. Navrotsky, B.J. Evans, *Physics and Chemistry of Minerals* 29 (2002) 515–526.
- [36] R.A. Robie, B.S. Hemingway, *U.S. Geological Survey Bulletin*, No. 2131, U.S.G.P.O., 1995.